Preparation and characterization of a novel luminescence nano-sillenite ($Bi_{12}SiO_{20}$) glass ceramic within Bi_2O_3–ZnO–SiO_2 system

Ola N. Almasarawi[1] · Esmat M. A. Hamzawy[1] · Fatma H. Margha[1] · Eglal R. Souaya[2] · Salwa A. M. Abdel-Hameed[1]

Abstract

Bismuth silicate with sillenite structure ($Bi_{12}SiO_{20}$) nanophase was prepared via melt–quenching technique in the Bi_2O_3–ZnO–SiO_2 glass system. The effect of replacement ZnO by Bi_2O_3 was studied. Their thermal behavior showed the change of glass transition temperature (Tg) from 577 °C in the Bi_2O_3-free glass to 438 °C in ZnO-free glass. In addition, the crystallization temperatures were not only changed from two to one peak, but also decreased from 927 to 476 °C in the same order. According to the heat treatment regimes, willemite, sillenite, tetragonal Bi_2O_3, cubic Bi_2O_3 and traces of ZnO were crystallized with different ratios depending on the change in composition and temperature. Sillenite was enhanced with increase heat treatment temperature and/or Bi_2O_3 additions. Heat treatment at 650 °C/10 h revealed the best regime, where higher degree of crystallization was achieved. The microstructure at 700 °C/30 min showed nano-scale oriented parallel rod crystals with hexagonal making at their end, whereas clusters of irregular nano-size crystals was appeared at 650 °C/10 h. Transmission spectra of the glasses in UV–Vis–midIR region were increased with Bi_2O_3 addition reaching 74% in 100B. Photoluminescence properties of both glasses and their corresponding glass–ceramics showed luminescence nature since the blue and green colors were clearly appeared. Calculation of optical bandgap (E_{opt}) revealed 3.2–2.19 eV with increasing Bi_2O_3; these values are located in the semiconducting range. The prepared samples can be utilized in electro-optical instruments, also the high transmission in mid-IR nominate it for IR transmitting windows.

Keywords Bismuth silicate glasses · Sillenite · Willemite · Nanostructure · Luminescence

1 Introduction

Bifunctional materials are ones that can perform two functions in a system due to their unique properties. Among the industries that utilize unique "smart" materials are energy, medical, nanoelectronics, aerospace, defense, semiconductors, and others. These materials have the potential to greatly improve new system performance by lowering size, weight, cost, power consumption, and complexity while also increasing efficiency, safety, and adaptability [1]. In comparison to commercially available semiconductors, the devices that use this smart material feature no instability, enlarged data

processing velocity, lower electric power, and high integration density [2].

In this paper, glasses and its counterpart glass ceramics have photoluminescence, and semiconducting characteristics were prepared. The compositions of glass ceramics were based on crystallization of both sillenite and willemite phases in varying amounts. The selection criteria for these phases were based on their interesting properties as will be explained later.

Sillenite phase has the formula $Bi_{12}MO_{20}$ where M = Si, Ti, Ge, Mn or some other IV-valence ion, or a mixture of the two ions. Lots of research has been done on both Ge and Ti-sillenite, where Gd-doped $Bi_{12}GeO_{20}$ sillenite has been prepared and showed antiferromagnetic interactions due to Gd cluster [3]. In addition, monophase $Bi_{12}TiO_{20}$ was crystallized in the system Bi_2O_3–TiO_2–SiO_2–Nd_2O_3 via melt-quenching process, and control the crystalline and amorphous phase formation was done [4]. Sillenite phase-stabilized multiphasic magnetoelectric Bismuth Ferrite was also prepared by employing different synthesis techniques namely soft chemical route

✉ Salwa A. M. Abdel-Hameed
  Salwa_nrc@hotmail.com

1 Glass Research Department, Dokki P.C., National Research Center, Cairo 12622, Egypt

2 Chemistry Department, Faculty of Science, Ain Shams University, Abbassia, Cairo 11566, Egypt

and rapid liquid phase sintering [5]. The principles density functional theory calculations of $Bi_{12}GeO_{20}$, $Bi_{12}SiO_{20}$, and $Bi_{12}TiO_{20}$ sillenites compounds were also calculated to determine its bonding and electronic structure [6]. On the other hands, academic researches on sillenites including band energy calculations of both BSO and BGO [7], photocatalytic effect of BTO [6, 8, 9], effect of pressure on BSO [10], and relative study of crystal structures of the three sillenites [11] were achieved.

Among all kinds of sillenite, bismuth silicon oxide (BSO) has attractive properties, especially photoconductive and electro-optical properties, so it has found application in a number of technically vital optical devices [12]. Sillenite ($Bi_{12}SiO_{20}$) exhibit piezoelectric, electro-optic, elasto-optic, photorefractive [12] and photoconductive properties, and so have potential applications in spatial light modulators, acoustic delay lines and hologram recording equipment.

$Bi_{12}SiO_{20}$ crystal is produced mainly by the Czochralski technique from the molten phase, although recently it was also prepared by the Bridgman method [13]. However, intrinsic defects such as core, striations and inclusions appear during crystal growth, degrading their optical quality and thus, require a means for their elimination [13].

On the other hand, willemite has the chemical formula Zn_2SiO_4. Scientists are interested in synthesizing it using various methods due to its use in various sectors. Willemite is classified as a useful phosphor because of its high luminous efficiency, great color purity, beside chemical and thermal stability [14, 15]. It was described as a down conversion luminous material [16] and a laser crystal [17]. It is also used as a chemically stable, transparent dielectric host for a variety of luminous dopants [18] and is a prominent component of crystalline glazes in modern ceramics [19].

Consequently, combination between the properties of both $Bi_{12}SiO_{20}$ with sillenite structure and willemite phases seem to be an aim worth trying, especially when prepared via traditional method as melt-quenching technique, where melt-quenching technique is well known on the industrial and laboratory scale, which makes it one of the best ways to prepare different materials.

In this regards, this study aim to crystallize $Bi_{12}SiO_{20}$ with different amount in $Bi_2O_3.ZnO.SiO_2$ glass system, via melt-quenching technique for the first time, where its production in glass ceramic using a simple and traditional method as a melt-quenching technique is object require to tray. Characterization of the prepared materials using DSC, XRD, TEM, optical as transmission and energy bandgap beside photoluminescence properties, were done.

2 Experimental and methods

2.1 Materials' preparation

Glasses in the system (100-x) $Bi_{12}SiO_{20}$. x Zn_2SiO_4, where x = 0–100, were prepared via melt-quenching method (Table 1). The samples were denoted 0B, 10B, 30B, 50B, 70B, 90B and 100B according to the amount of $Bi_{12}SiO_{20}$. About 30 g of the powder of these compositions were prepared from reagent grade SiO_2, Bi_2O_3 and ZnO. After mixing for 15 min to facilitate the melting process and make better glass homogeneity, the batches were melted in a porcelain crucible in an electrical furnace at a temperature range (950–1200 °C) for 0.5 h with occasional swirling to make sure homogenization. The melts were poured onto a stainless-steel plate at room temperature and pressed into a plate 1–2 mm thick by another cold steel plate.

2.2 Materials characterization

The thermal behaviors (differential scanning calorimetric analysis DSC) of the finely powdered quenched samples were examined using TG-DSC SETARAM Instrumentation Regulation, Labsys TM (Setaram, Caluire, France) under inert gas (N_2 with purity 99.99%) with flow rate 60 cm^3/min. The powder (10–15 mg) was heated in Pt-holder with another Pt-holder containing Al_2O_3 as a reference material. As will be shown later, the acquired data were used as a guide to establish the requisite heat treatment temperatures to induce the crystallization in the samples.

To determine the kinds and relative amounts of the crystalline phases, quenched samples were subjected to powder X-ray diffraction using Bruker diffractometer (Germany D8 ADVANCE Cu target 1.54 Å, 40 kv, 40 mA) with graphite monochromatized Ni-filled Cu-Kα radiation. JCPDS X-ray diffraction card files were used to obtain reference data for interpreting the X-ray diffraction patterns.

To characterize the nanocrystals' size, distribution and morphology, high-resolution transmission electron

Table 1 Chemical composition of the prepared glasses in mole%

Sample code	Bi_2O_3	SiO_2	ZnO
0B	–	33.33	66.66
10B	17.647	29.4116	52.9412
30B	42.8572	23.8094	33.3332
50B	60.0002	19.9997	19.9999
70B	72.4142	17.2412	10.3445
90B	77.1431	14.2854	8.5713
100B	85.7143	14.2856	–

Table 2 XRD results of the prepared glass ceramics

Sample code	Heat treatment	Phases
0B	650 °C/30 min	Willemite + ZnO
10B		–
30B		Sillenite
50B		Sillenite + T-Bi_2O_3
70B		Sillenite + T-Bi_2O_3
90B		Sillenite + T-Bi_2O_3
100B		Sillenite + T-Bi_2O_3
0B	650 °C/10 h	Willemite + ZnO
10B		Willemite + sillenite
30B		Sillenite + C-Bi_2O_3
50B		Sillenite + C-Bi_2O_3
70B		Sillenite + T-Bi_2O_3
90B		Sillenite + T-Bi_2O_3
100B		Sillenite + T-Bi_2O_3
0B	700 °C/30 min	Willemite + ZnO
10B		Willemite
30B		C-Bi_2O_3
50B		Sillenite + T-Bi_2O_3
70B		Sillenite + T-Bi_2O_3
90B		Sillenite + T-Bi_2O_3
100B		Sillenite
0B	800 °C/30 min	Willemite + ZnO
10B		Willemite + sillenite
30B		Willemite + sillenite
50B		Willemite + sillenite
70B		Willemite + sillenite
90B		–
100B		Sillenite

microscope HRTEM (JEOL JEM-2100 at an accelerating voltage of 200 kV, attached to CCD camera) is used.

The optical transmittance spectra of all the glasses were recorded at room temperature using a model JASCO Corp-V-570 spectrometer in the wavelength range 200–2400 nm in the ultraviolet–visible–mid-IR parts of the spectrum. The experimental data are expressed as optical percent transmission as a function of wavelength in nanometers (nm). The values of optical bandgap (E_{opt}) have been determined from the cutoff wavelength of these glasses.

Photoluminescence measurements of the prepared glasses and their corresponding glass ceramics were recorded at room temperature under the excitation wavelength range of 200–450 nm in the spectral range 400–750 nm using a fluorescence spectrophotometer (type JASCO, FP-6500, Japan) equipped with a xenon flash lamp as the excitation light source. The scan speed is 0.15 with a step length of 0.25 nm and a slit width of 0.2 nm.
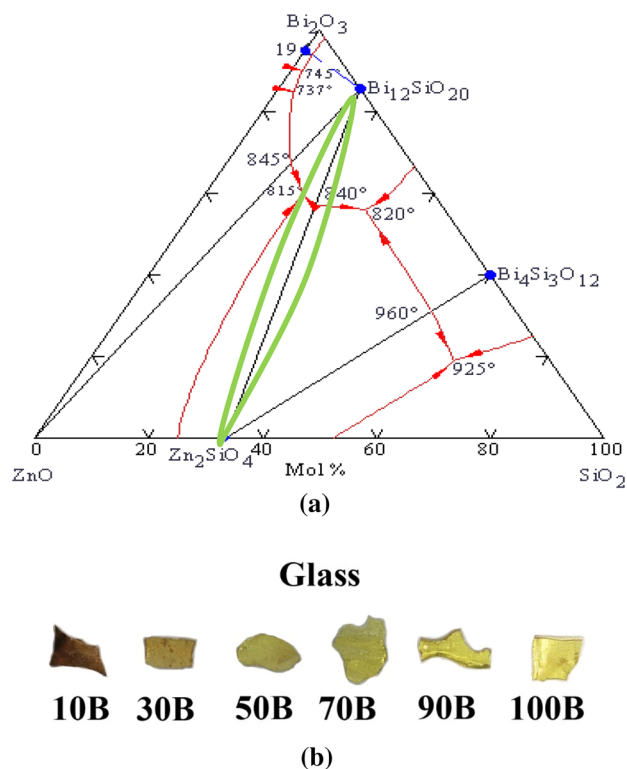

Fig. 1 **a** Phase diagram between Bi_2O_3, SiO_2 and ZnO, the line between the green arcs is the chosen one for this study [11] and **b** visual image for the prepared glasses

3 Results and discussion

Phase diagram between Bi_2O_3, SiO_2 and ZnO [21] is illustrated in Fig. 1a. In this study, the focus was on the line between sillenite ($Bi_{12}SiO_{20}$) and willemite (Zn_2SiO_4). Seven compositions were chosen on this line, and denoted as 0B, 10B, 30B, 50B, 70B, 90B and 100B, where the number expressed the mole percent of sillenite (Table 1). Figure 1b represents the visual images for the prepared glasses.

3.1 DSC analysis

DSC analyses for the as-prepared glasses are illustrated in Fig. 2. Through DSC analysis, important data were achieved, such as glass transition temperature (Tg) at which the viscosity of the glass is slightly decreased; as a result, this step is associated with an increase in heat capacity [22], and crystallization temperature (Tc) which is related to an irreversible phase change, thus this step is associated with a decrease in heat capacity [22]. In this study, clear endothermic effects (Tg) are appearing in the temperature range 438–577 °C; while two exothermic peaks are appeared in the range 466–673 °C and 575–927 °C for glasses 0B–70B. With increasing Bi_2O_3, the two exothermic peaks are reduced and gathered in one exothermic peak, in the range
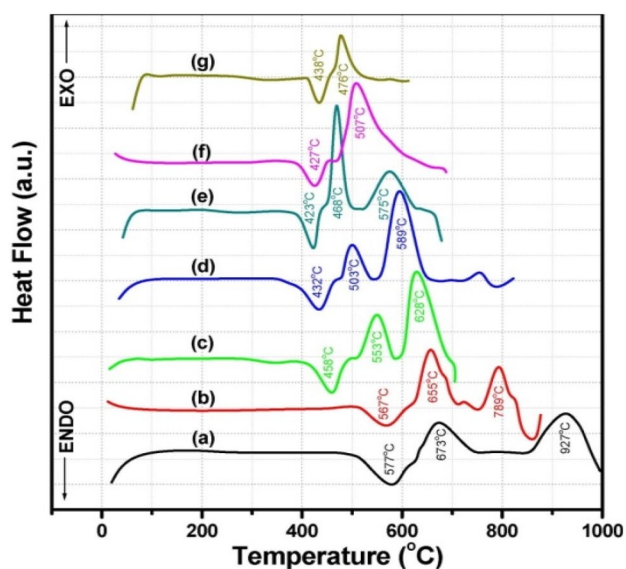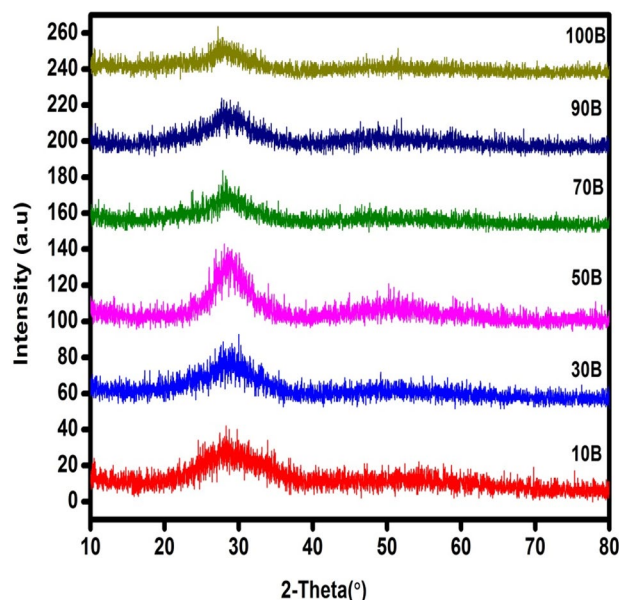
Fig. 2 DSC thermograms of as-prepared samples **a** 0B, **b** 10B, **c** 30B, **d** 50B, **e** 70B, **f** 90B and **g** 100B

Fig. 3 XRD patterns of as-prepared glass samples

476–507 °C, as in 90B and 100B. It is noticed that both Tg and Tc are decreased with increasing Bi_2O_3 additions.

From Table 1, Bi_2O_3 was increased, while both SiO_2 and ZnO were decreased, from 0B to 100B. The bond energy of Si–O which is 452 kJ/mole is higher than Bi–O, which records 343 kJ/mole [12]. The bond energy is directly related to bond strength; consequently, the Si–O bond is stronger than the Bi–O bond, which leads to a more compact and viscous structure. Thus, as Bi_2O_3 increased, as the weak Bi–O bond increased and the energy needed to break it decreased, consequently Tg temperature becomes inversely proportional to the amount of Bi_2O_3 [23]. From another point of view, SiO_2 is presented in the glass structure as SiO_4 unit, while Bi_2O_3 is presented as both BiO_3 and BiO_6 units. BiO_n unit is shared through their edges so it is more or less distorted link [24], while the tetrahedral SiO_4 were linked through oxygen atoms of corners forming chains, sheets, or three-dimensional networks [25, 26]. Consequently, increasing SiO_2 content led to increase in Si–O–Si bridges which improves glass stability, whereas in samples with high bismuth content, the majority of oxygen atoms form Bi–O–Bi and Si–O–Bi bonds, with a smaller number from Si–O–Si bonds in SiO_4 chains [27].

On the other hands, increasing the percentage of Bi_2O_3, at the expense of ZnO, led also to a decrease in the Tg and Tc temperatures. This might be explained by the stronger effect of Bi_2O_3 to lowering the glass transition temperature, as discussed before, i.e., weakening the glass network structure compared with ZnO, where the single bond strengths of Zn–O bonds in ZnO_4 groups are higher than that for Bi–O bonds in BiO_6 groups[28]. Thus, Bi–O–Bi cross-linkages are broken easily to form non-bridging oxygen in the glass

matrix, leading to easier mobility of the ions and decrease both Tg and Tc [29].

The exothermic peaks are related to crystallization temperature Tc; the presence of two peaks may be means crystallization of two phases in different temperature ranges; while one exothermic peak mean one or more crystalline phases in the same temperature range. The decrease in Tc temperature with increasing Bi_2O_3 was explained before; whereby adding Bi_2O_3, the glassy phase's stability towards crystallization is reduced, resulting in a decrease in the crystallization temperature.

3.2 X-ray diffraction

Glass samples are exposed to different heat treatment programs as 650 °C/30 min, 700 °C/30 min, 800 °C/30 min and 650 °C/10 h. The different programs are applied to study the effect of heat treatment parameters on the sequence of crystallization, phases developed and stability toward increasing temperature. XRD patterns of the studied samples before and after different heat treatment programs are shown in Figs. 3, 4 and 5. The developed phases are illustrated in Table 2.

X-ray of the as received glasses shows a clear hump within 25–35 2Θ which conformed the amorphous phase (Fig. 3). After heat treatment (Fig. 4), XRD diffractograms demonstrated the formation of willemite (JCPDS 70–1235), sillenite (JCPDS 37–0485 or 17–0804), tetragonal Bi_2O_3 (JCPDS 78–1793), cubic Bi_2O_3 (06–0132) and ZnO (JCPDS 89–0510). Details of XRD for each sample, with different heat treatment schedules, will be explained as follows.

Fig. 4 XRD patterns of 10B–100B glass samples after different heat treatment schedules
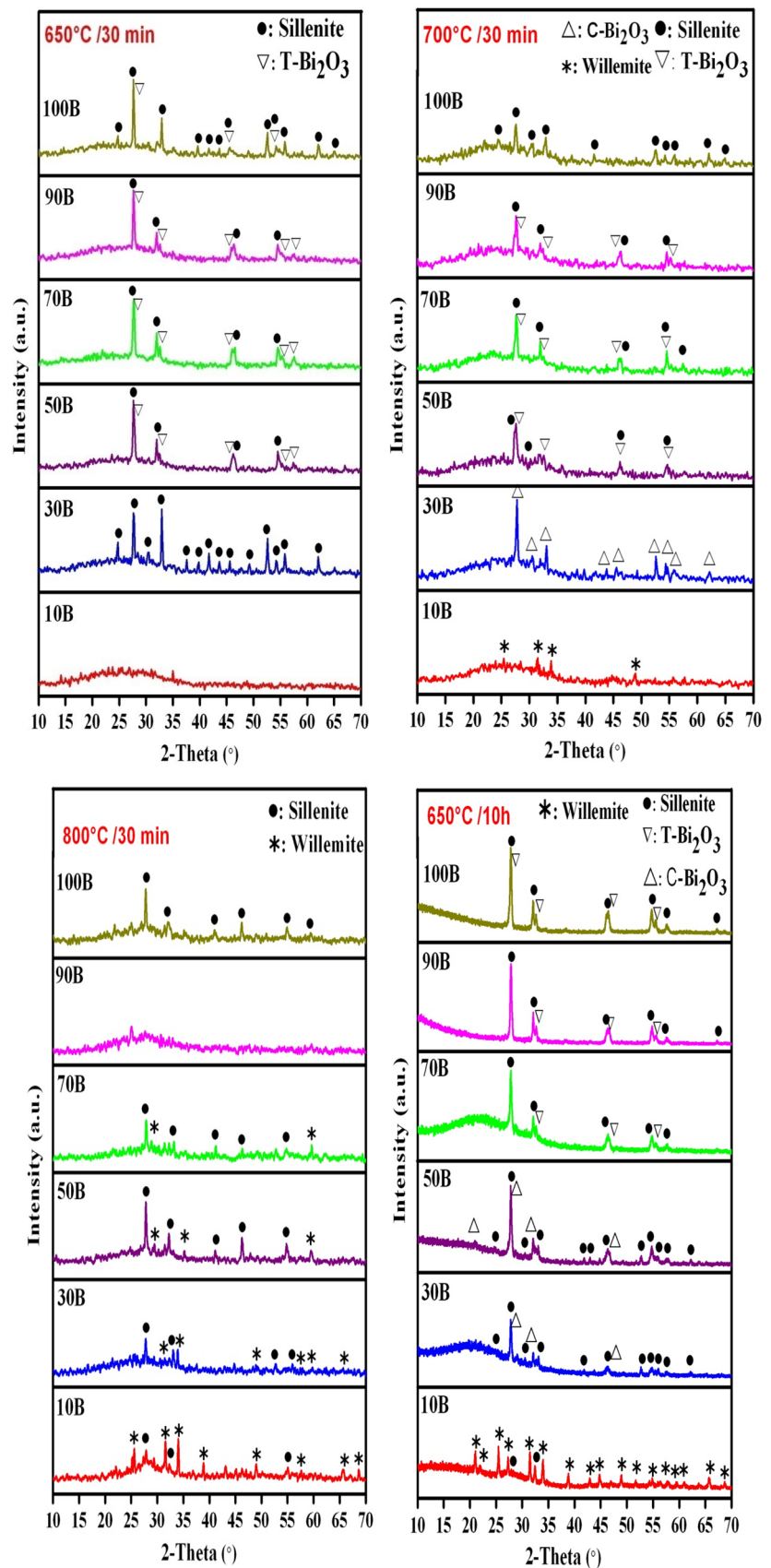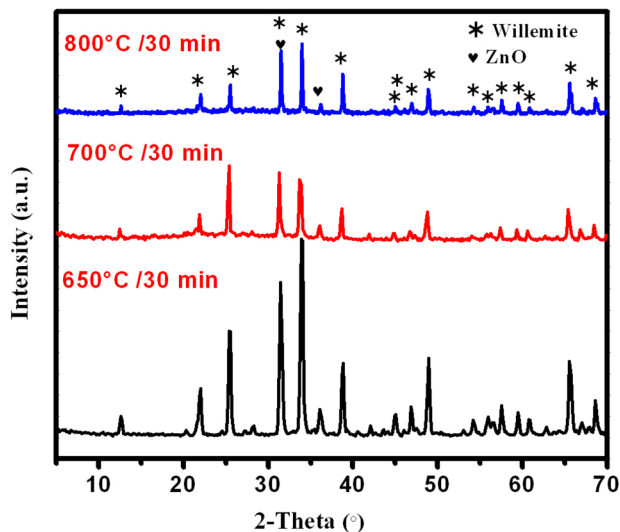
Fig. 5 XRD patterns of 0B glass samples after different heat treatment schedules

At 650 °C/30 min, the time seems not enough to crystallize willemite in all glass compositions. In 10B, the amount of Bi_2O_3 is too low to react with SiO_2 to give sillenite or precipitate as Bi_2O_3; consequently, amorphous phase is the feature for 10B. By increasing the addition of Bi_2O_3, crystallization of pure body-centered cubic (JCPDS 37–0485) sillenite in 30B is achieved, where all Bi_2O_3 are reacted with the required SiO_2 amount to give sillenite. Increasing the Bi_2O_3 in 50B–100B revealed more development for sillenite beside relatively lower amount from $T-Bi_2O_3$. The crystallized sillenite here is the face-centered cubic one (JCPDS 17-0804). Consequently, the mechanism of crystallization may be as follows: at the first, Bi_2O_3 was reacted with a suitable amount of SiO_2 to form body-centered cubic sillenite, which converted to face-centered one with increasing Bi_2O_3. More addition of Bi_2O_3 leads to precipitation of the excess amount of Bi_2O_3 as $T-Bi_2O_3$.

Increasing the heat treatment temperature to 700 °C for 30 min shows crystallization of pure willemite in 10B, pure $C-Bi_2O_3$ in 30B, and then equal amounts from sillenite and $T-Bi_2O_3$ in 50B. Sillenite was increased and $T-Bi_2O_3$ was decreased with increasing Bi_2O_3 in 70B and 90B. Only sillenite phase was developed in 100B. It is noticed that the peaks' intensity decreased with increasing Bi_2O_3 referring to partial melting was occurred. The $C-Bi_2O_3$ phase is easier in formation than $T-Bi_2O_3$; furthermore, it converted into $T-Bi_2O_3$ with increasing Bi_2O_3 ratio. The transformation from cubic to tetragonal Bi_2O_3 phase can be attributed to the reformation of the disordered truncated octahedral BiO_5 and tetrahedral BiO_4 units, which are the building blocks of the cubic structure [30].

Increasing the temperature of heat treatment to 800 °C for 30 min revealed the crystallization of willemite as major phase and sillenite as minor one in 10B. With increasing Bi_2O_3, sillenite was increased to be the major phase and willemite became the minor one in 30B–70B. Pure sillenite is appeared in 100B. The decrease in peaks' intensity than previous heat treatment revealed more partial melting in these samples. Abnormal result was noted, where sample 90B was more remelted than 100B; this may be due to that Bi_2O_3 can act as both glass modifier or former according to its amount, and at lower quantity, it acts as modifier and form BiO_6 unit. With increasing its quantity, BiO_6 is decreased while BiO_3 unit increased, hence Bi_2O_3 mainly acted as glass former, so more compact structure was observed in 100B [31].

Heat treatment at 650 °C/10 h with heating rate 1 °C/min was applied to study the effect of increasing time with slow rate in the crystallization process; in general, it revealed well-crystalline phases which is mirrored by high peak intensity and lower background noise. Well-developed willemite and traces from sillenite in 10B are presented. Both sillenite and $C-Bi_2O_3$ are crystallized in 30B and 50B, while $C-Bi_2O_3$ is converted to $T-Bi_2O_3$ one by increasing Bi_2O_3 in 70B, 90B and 100B beside the major crystallized sillenite phase.

According to XRD results, heat treatment at 650 °C/10 h with heating rate 1 °C/min revealed the most intense and sharp XRD Braggs peaks, which reflect more degree of crystallization of the desired phases, without partial remelting, so it will be considered in the followed characterizations.

The X-ray chart of the bismuth-free sample (0B) is separated from the rest samples because it showed a special behavior (as given in Fig. 5). As clarified willemite and ZnO were crystallized at different heat treatment schedule, these phases are expected where ZnO reacted with SiO_2 to give willemite, and the excess is precipitated as ZnO.

Figure 6a and b represents 3-dimensional structure of both sillenite and willemite in the same order. Figure 6a depicts the local structure around Bi (BiO_7 irregular polyhedron) and around Si ion (SiO_4 tetrahedron); these results are matched with the literature [6]. Figure 6b represents 3-dimensional structure of willemite (Zn_2SiO_4) indicating four- and six-membered rings of ZnO_4 and SiO_4 tetrahedra. The present simulated 3d structure is matched with that reported in the previous study [32].

3.3 Transmission electron microscope (TEM)

HRTEM was used to study the microstructure of the obtained nano-glass ceramics heat-treated at both 700 °C/30 min and 650 °C/10 h. TEM images and the corresponding selected area electron diffraction (SAED) patterns are presented in Figs. 7 and 8 in the same order. After heat treatment at 700 °C/30 min (Fig. 7), the microstructure of 10B represents

(a)

(b)
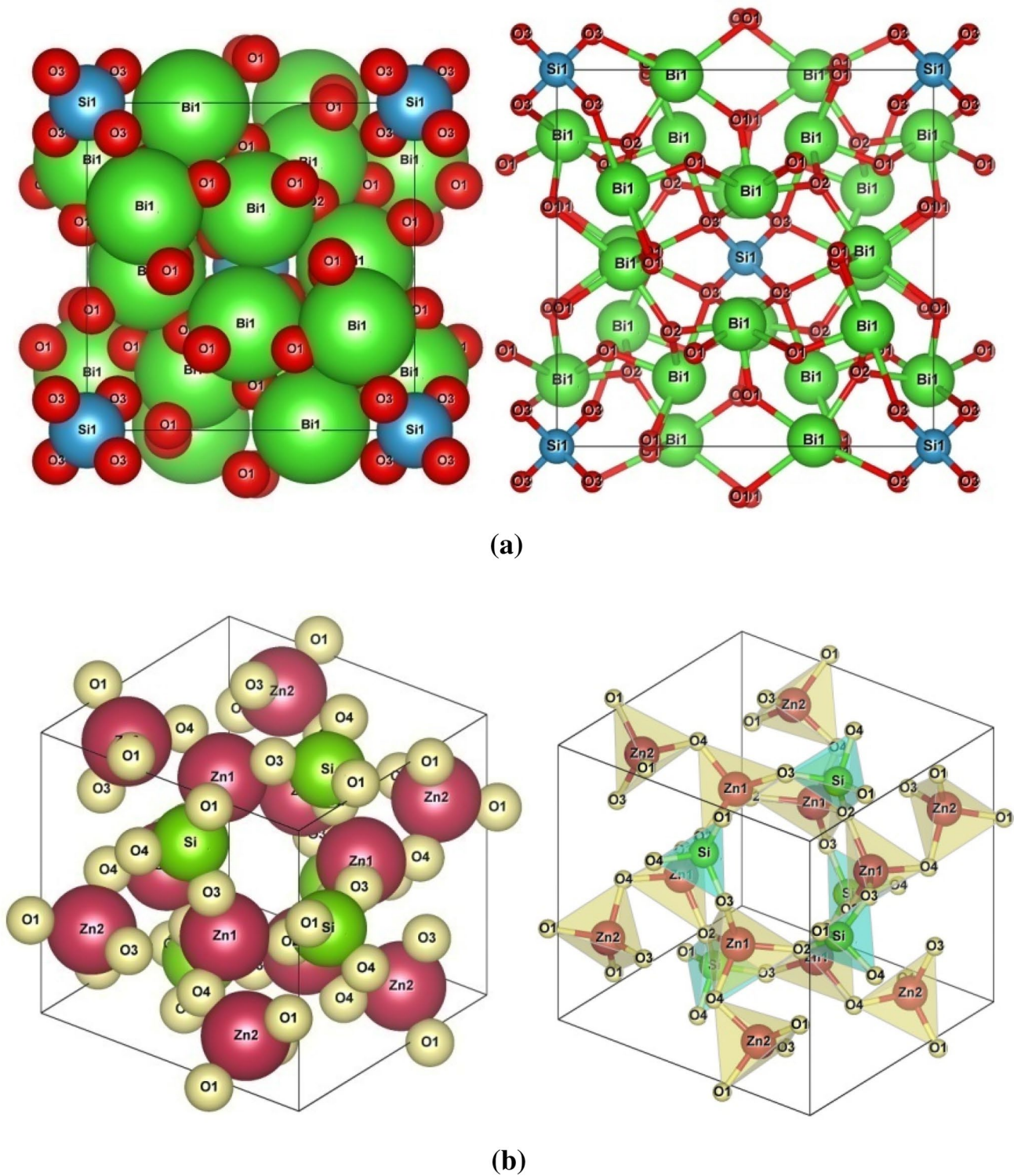
Fig. 6 Crystal structure of **a** sillenite and **b** willemite

one crystalline phase with a rhombohedral structure having different directions corresponding to willemite phase; the crystals are dense and translucent with crystallite size ~ 8 nm. The translucent character of the crystals can be revealed to the crystallization process where the crystallization is going in two dimensions only (2D). Therefore, the crystallites appear as sheets, i.e., have not the 3rd dimension and, consequently, appeared translucent. SAED revealed a

Fig. 7 TEM for the prepared samples after heat treatment at 700 °C/30 min
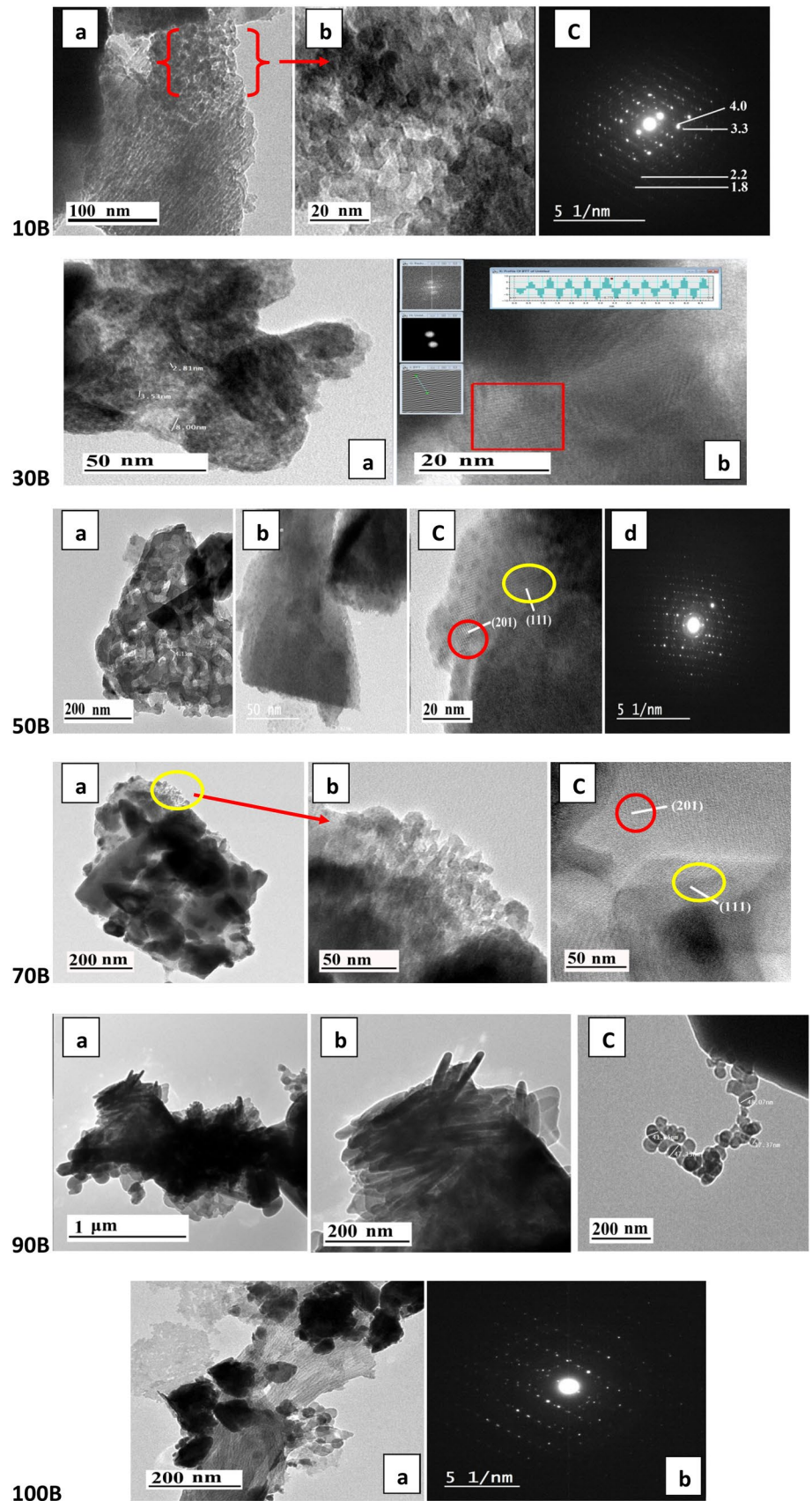
Fig. 8 TEM for the prepared samples after heat treatment at 650 °C/10 h
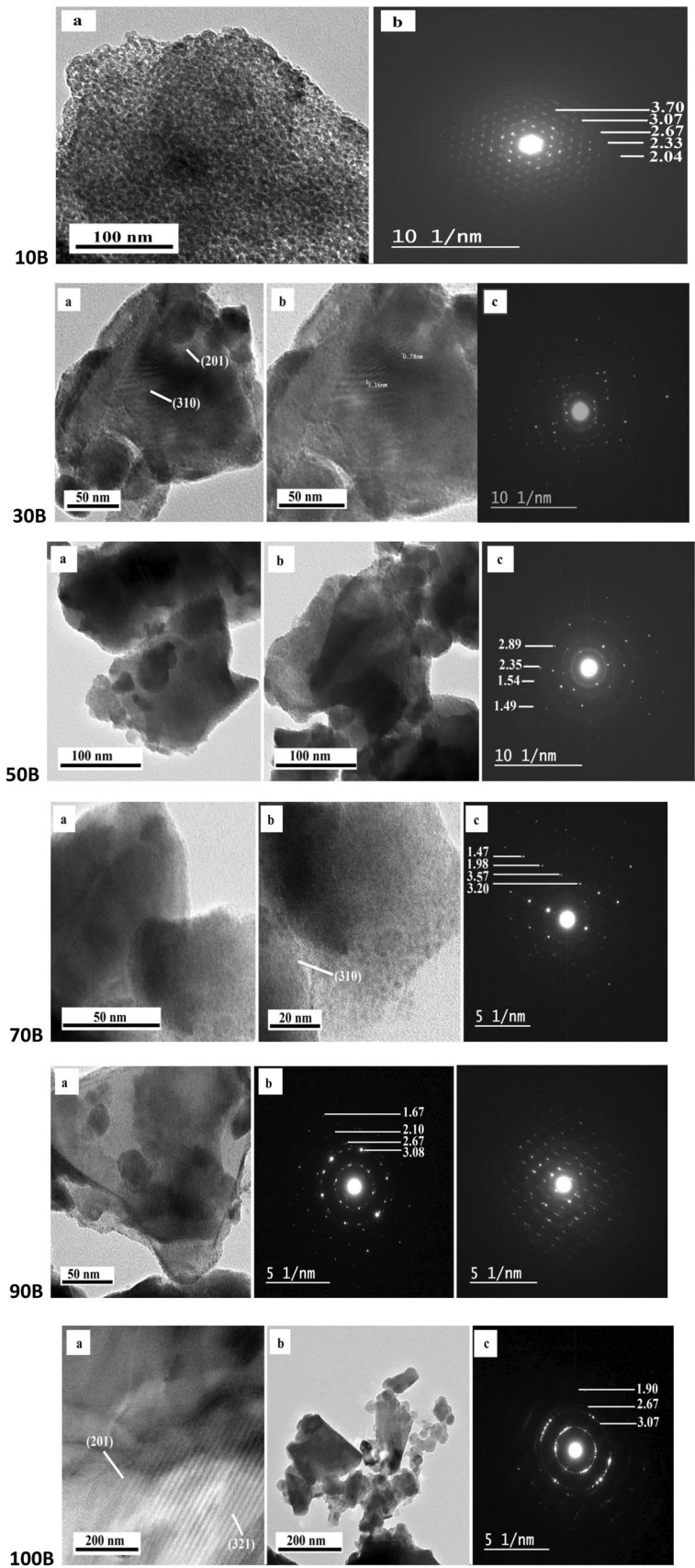
uniform pattern corresponding to pure crystalline phase with d-spacing = 4, 3.3, 2.2 and 1.8 Å corresponding to hkl 121, 220, and 223, respectively, of willemite. 30B revealed pure crystalline phase with crystallite size ~ 5 nm corresponding to C-Bi_2O_3 and interplanar spacing d value is about 2.8 nm corresponding to (222) crystal plane of C-Bi_2O_3.

50B revealed two crystalline shapes; one is dense and translucent with size ~ 5 nm corresponding to sillenite and the other is rounded with crystallite size ~ 2 nm correspond to T-Bi_2O_3; SAED revealed uniform pattern and clear-cut crystalline lattice structure whose interplanar spacing values are matched with the crystallized phases detected by XRD. 70B revealed more sillenite crystals (~ 5 nm) with clear-cut crystalline lattice structure. 90B gives more development for both sillenite as major phase and T-Bi_2O_3; sillenite is appeared as well-round crystal with size ~ 40 nm and T-Bi_2O_3 is appeared as elongated fiber crystals with width ˷23 nm. 100B depicted uniform SAED corresponding to the single crystalline phase of sillenite with crystallite size ~ 20 nm. In general, all TEM micrographs contain predominantly translucent thin sheet shaped morphology, i.e., layered microstructure, of nano-crystallites.

TEM image of glass ceramic after heat treatment at 650 °C/10 h with heating rate 1 °C/min is shown in Fig. 8. 10B revealed homogenous and dense crystallization of willemite with crystal size ~ 5 nm and uniform SAED pattern with interplanar spacing value matched with d-spacing of willemite. Both 30B and 50B revealed SAED and HRTEM of polycrystalline phases with interplanar d-spacing matched with sillenite and C-Bi_2O_3; both phases are composed of rounded crystals of ~ 3 nm size. TEM for 70B–100B revealed very tiny crystals with crystal size ~ 5–30 nm. SAED and HRTEM images show polycrystalline phases with interplanar d-spacing matching with sillenite and T-Bi_2O_3.

3.4 Optical properties

The optical transmission spectra curves in UV–visible–mid-IR region from 200 to 2500 nm for the as-prepared glasses are shown in Fig. 9. It is observed that optical absorption edge is not sharply defined, which indicates the amorphous nature of the samples [8]. It is also observed that the cutoff wavelength (k_{cutoff}) decreases as the content of SiO_2 increases in the glass system. According to many previous studies [33–37], the detected ultraviolet–near visible peaks in Fig. 9 can be attributed to the presence of heavy massive bismuth ions, which allow the $^1S_0 \rightarrow ^3P_1$ transition of Bi^{3+} ions.

In general, bismuth glasses are characterized by their transparency in the IR region from 0.8 to 2.5 μm [22]. The prepared samples are characterized by two transmission regions, one in the UV–Vis–mid-IR range where the transmission increased sharply with increasing wavelength
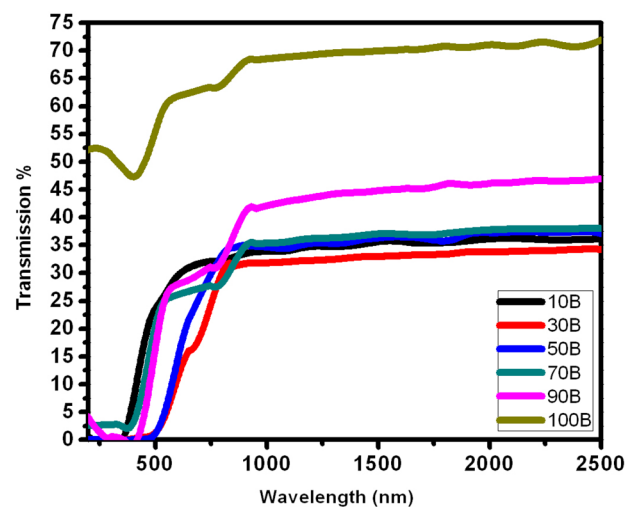

Fig. 9 UV–Vis–mid-IR transmission curves for different glasses

till ~ 900 nm reaching 36–38% for 10B–70B; however, for 90B and 100B it increased sharply to reach 46 and 72%, in the same order. After that, almost steady state from 900 to 2500 nm was appeared. Consequently, these glasses are promising materials for photonic applications, IR transmission windows and communication purposes [38].

In an amorphous system, the optical bandgap energy (E_{opt}) is strongly connected to the energy gap between the valence and conduction bands [39]. The glass forming anions have the most influence on the conduction band. The absorption coefficient near the absorption curve's edge was used to calculate the optical bandgap energy of the prepared glasses (Fig. 10). The absorption coefficient was calculated using the formula:

$\alpha = 2.303A/t$ [18]

where A is the absorbance and t is the sample thickness in centimeters. The following equation describes the relationship between α and the photon energy of the incident radiation, hν. [24]:

$\alpha h\nu = B (h\nu - E_{opt})^r$

where B is the constant, E_{opt} is the optical bandgap energy and *r* is an index equal to 2, 3, 1/2 or 3/2, according to the indirect allowed or forbidden and direct allowed or forbidden transitions, respectively [40]. Here, $r = 2$ where the most transition in all amorphous solids is an indirect allowed transition [40]. The E_{opt} values are determined by the extrapolation of the linear region of the plot of $(\alpha h\nu)^2$ vs hν. The obtained values of E_{opt} are in the range 3.24–2.19 eV, i.e., within the semiconductor range; it decreases with increasing Bi_2O_3 content.

The optical bandgap (E_{opt}) is mainly depending on to the network structure's compactness. As the number of bridging atoms increases, the glass network becomes more compact, and the optical bandgap values enhanced [23]. As
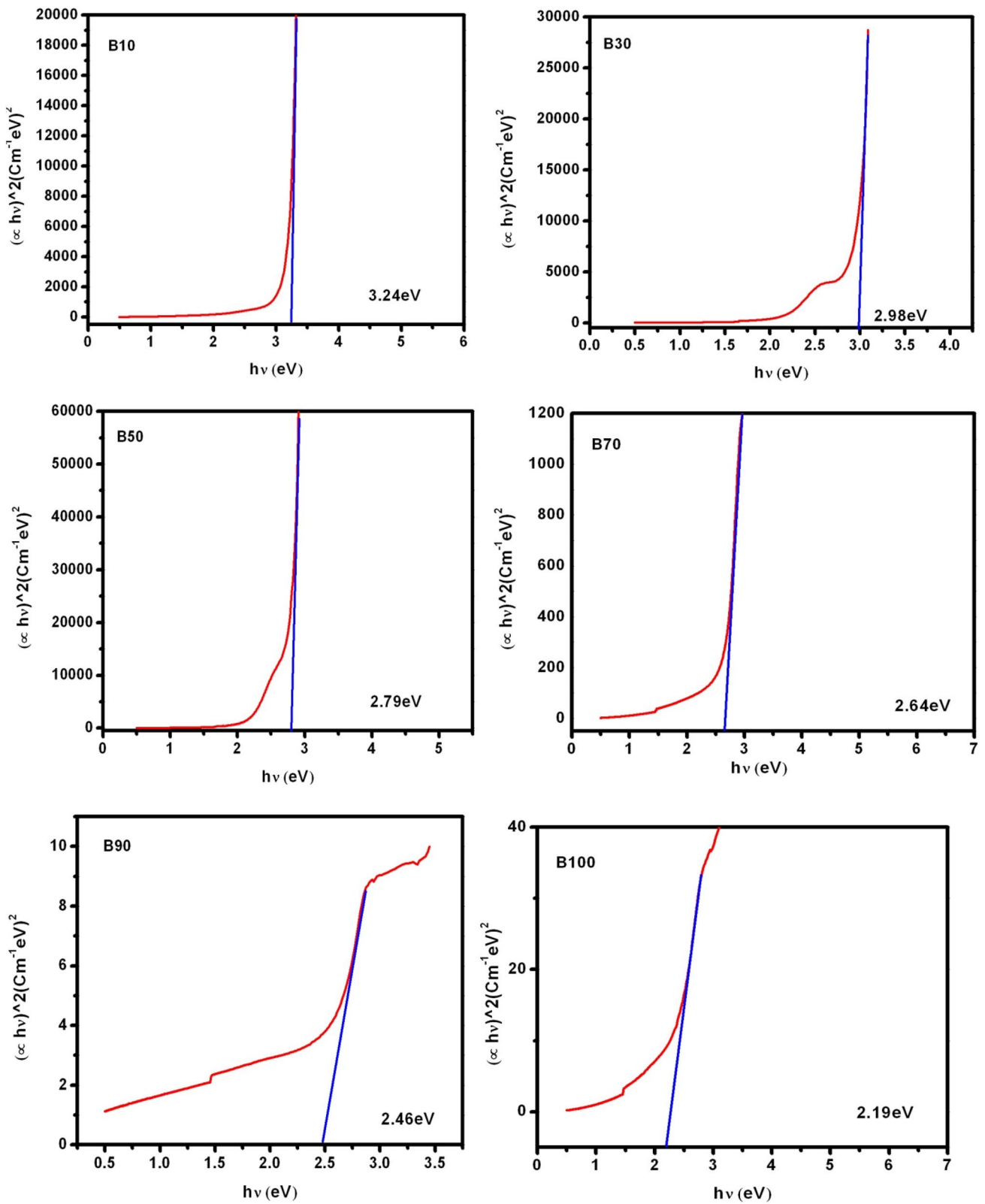
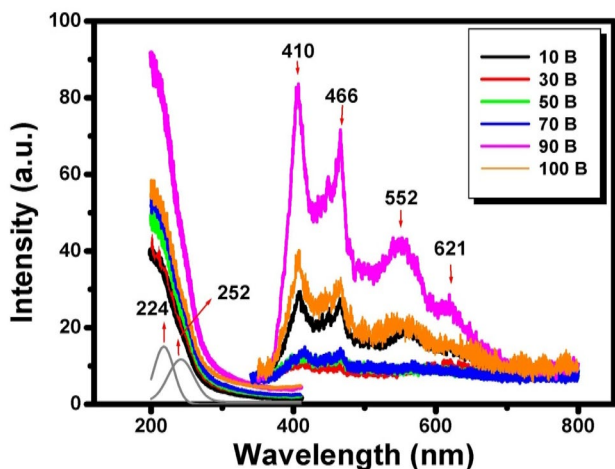**Fig. 10** Optical bandgap energy for as-prepared samples

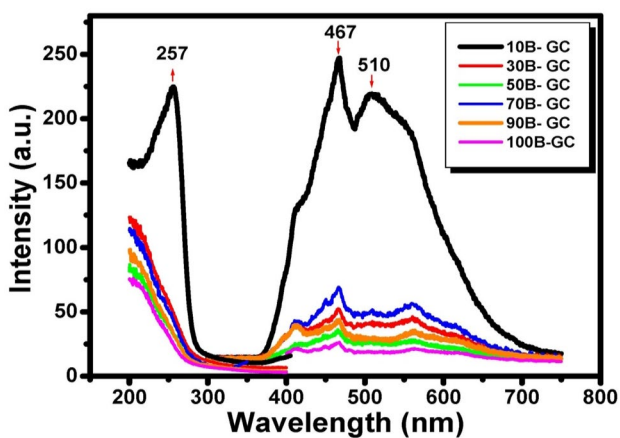Fig. 11 Photoluminescence measurements for as-prepared samples

Fig. 13 CIE diagram for both glass and glass ceramics

Fig. 12 Photoluminescence measurements for glass ceramic after heat treatment at 650 °C/10 h
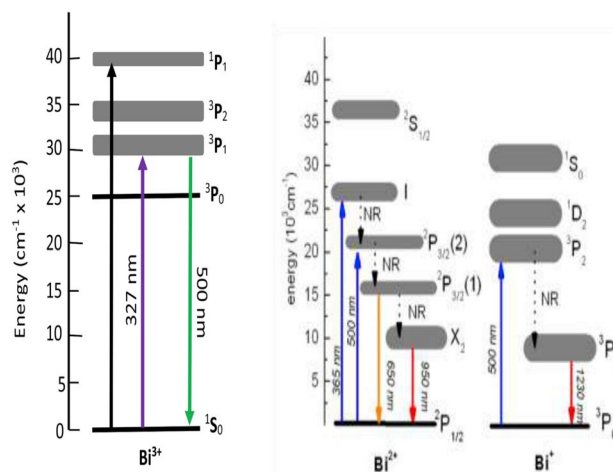
Fig. 14 Simplified energy level diagram for Bi^{3+}, Bi^{2+} and Bi^+ [24]

previously noted, the addition of both ZnO and SiO_2 to this glass composition resulted in stronger oxygen bonding than in the case of Bi_2O_3, resulting in a tighter texture in sample 10B than in samples 100B with the lowest SiO_2 content and zero ZnO. As a result, substituting Bi_2O_3 for SiO_2 in this glass composition reduces the optical bandgap (E_{opt}). From another perspective, the drop in phonon-assisted indirect transitions reflects the decrease in optical bandgap energy [1]. In general, all optical bandgap (E_{opt}) values are in the semiconductor area.

3.5 Photoluminescence measurements

The photoluminescence (PL) spectra and CIE diagram of the glasses and their corresponding glass ceramics at excitation wavelengths 224 and 257 nm, respectively, at room temperature are shown in Figs. 11, 12 and 13. PL for different
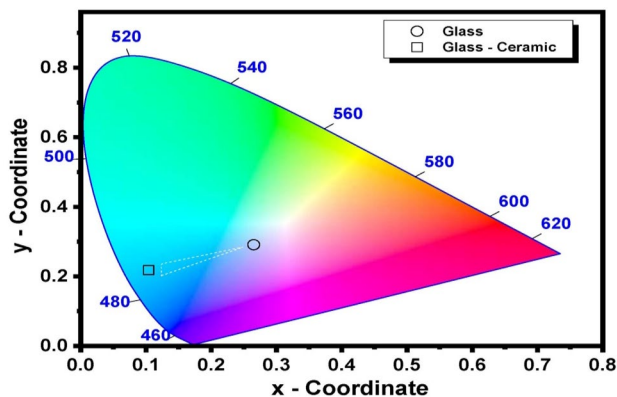
glasses revealed four emission peaks, two intense and sharp at 410 (violet), 466 (blue) and two broads at 552 (green) and 621 nm (orange); the combination between these colors gives pale purple as depict from CIE diagram. The PL of heat-treated samples at 650 °C/10 h at $\lambda_{ex} = 257$ nm revealed significant enhancement of emission intensity at 467 (blue) and 510 nm (green). The submission of these two colors gives cyan color as depicted from CIE diagram.

Bismuth is a non-toxic post-transition metal with a wide variety of valence states, which, along with its proclivity for cluster formation, makes it a versatile but difficult dopant for possible luminescence applications. Since the outer orbitals responsible for luminescence are not insulated and are heavily impacted by their surroundings, their energies are host dependent [32]. Bismuth-based compounds have a wide range of luminescence, ranging from UV to infrared emissions. The energy level diagram for Bi^{3+}, Bi^{2+} and Bi^+ [19] is presented in Fig. 14. The outer orbital responsible for

luminescence is unshielded and heavily impacted by the surrounding environment, resulting in a host-dependent energy, comparable to the f–d transitions of Ce^{3+} and Eu^{2+} ions, which change depending on the host. This allows Bi^{3+} ions to emit light over a wide variety of wavelengths, which adds to its appeal as a luminescent center.

4 Conclusions

1- Nano-crystalline sillenite glass ceramic was prepared by melting quenching technique in the system ZnO–SiO_2–Bi_2O_3 by adding Bi_2O_3 on the expense of ZnO and SiO_2. Addition of Bi^{3+} leads to decrease both Tg and Tc temperature.

2- The XRD revealed that the sillenite phase was enhanced with both temperature and the amount of Bi_2O_3 added.

3- TEM and SAED images perform the formation of both rhombohedral structure of willemite (~ 8 nm) and dense and translucent hexagonal shape of sillenite (~ 5 nm)

4- The transmission in UV–Vis–mid-IR reaches 74% in 100B, which nominate it for IR transmission windows. The optical bandgap (E_{opt}) values are in the ranges 3.24–2.19 eV for all glasses, i.e., in semiconducting range. PL emissions spectra revealed pale purple color and cyan for the glass and glass ceramic samples, respectively.

5- Therefore, the prepared glasses are considered promising materials for photonic applications, communication purposes and as a semiconductor.

Data availability The data is available when required.

Declarations

Conflict of interest The authors confirm that there are no conflicts of interests.

References

1. Y. Bar-Cohen, *Biomimetics: Biologically Inspired Technologies* (CRC Press, Boca Raton, 2005)
2. S. Emura, M. Takahashi, H. Tambo, A. Suzuki, T. Nakamura, Y.-K. Zhou, S. Hasagawa, H. Asahi, MRS Online Proceedings Library (OPL) **1111**, (2008).
3. S. Simon, A.D. Udvar, J. Am. Ceram. Soc. **93**, 2760 (2010)
4. S. Slavov, Z. Jiao, *Journal of Physics: Conference Series* (IOP Publishing, Bristol, 2018), p.012040
5. K.S. Sivaraj, K.S. Sreehari, R.N. Bhowmik, M.R. Anantharaman, J. Solid State Chem. **299**, 122162 (2021)
6. S.A.S. Farias, J.B.L. Martins, Chem. Phys. Lett. **533**, 78 (2012)
7. I.V. Kityk, M.K. Zamorskii, J. Kasperczyk, Phys. B Condens. Matter **226**, 381 (1996)
8. J. Lu, Y. Dai, Y. Zhu, B. Huang, Chem. Cat. Chem. **3**, 378 (2011)
9. J. Zhou, Z. Zou, A.K. Ray, X.S. Zhao, Ind. Eng. Chem. Res. **46**, 745 (2007)
10. W. Wei, Y. Dai, B. Huang, J. Phys. Chem. C **113**, 5658 (2009)
11. L. Wiehl, A. Friedrich, E. Haussühl, W. Morgenroth, A. Grzechnik, K. Friese, B. Winkler, K. Refson, V. Milman, J. Phys. Condens. Matter **22**, 505401 (2010)
12. A.F. de Lima, S.A.S. de Farias, M.V. Lalic, J. Appl. Phys. **110**, 083705 (2011)
13. C. Shen, H. Zhang, Y. Zhang, H. Xu, H. Yu, J. Wang, S. Zhang, Crystals (Basel) **4**, 141 (2014)
14. A.V. Golubović, S.N. Nikolić, R. Gajić, S. Đurić, A. Valčić, J. Serb. Chem. Soc. **67**, 279 (2002)
15. N. Sangwaranatee, S. Tuscharoen, H.J. Kim, J. Kaewkhao, Mater Today Proc. **5**, 15061 (2018)
16. M.-Y. Chen, J. Juuti, C.-S. Hsi, H. Jantunen, J. Eur. Ceram. Soc. **37**, 1495 (2017)
17. J. Cimek, R. Stępień, M. Klimczak, I. Zalewska, R. Buczyński, Opt. Mater. (Amst.) **73**, 277 (2017)
18. R. Bala, A. Agarwal, S. Sanghi, N. Singh, Opt. Mater. (Amst.) **36**, 352 (2013)
19. H.C. Swart, R.E. Kroon, Opt. Mater. X **2**, 100025 (2019)
20. M.-Y. Chen, J. Juuti, H. Jantunen, J. Alloy. Compd. **737**, 392–397 (2018)
21. V. M. Skorikov, R. Z. A. Z. PF, D. FF, (1981)
22. S.A.M. Abdel-Hameed, A.M. Fathi, M. Eltohamy, J. Non Cryst. Solids **510**, 71 (2019)
23. Y.-R. Luo, *Comprehensive Handbook of Chemical Bond Energies* (CRC Press, Boca Raton, 2007)
24. W. Adam, W. Agnieszka, B. Michał, R. Jarosław, F. Sandro, F. Sandro, C. Giancarlo, CMST **10**, 203 (2004)
25. W.H. Zachariasen, J. Am. Chem. Soc. **54**, 3841 (1932)
26. P. Manuel, I. Rajasingh, A. William, and A. Kishore, in *Proceedings of the International Conference on Parallel and Distributed Processing Techniques and Applications (PDPTA)* (The Steering Committee of The World Congress in Computer Science, Computer, 2011), p. 1
27. M. Todea, R.V.F. Turcu, M. Vasilescu, D.L. Trandafir, S. Simon, J. Non Cryst. Solids **432**, 271 (2016)
28. T. Inoue, T. Honma, V. Dimitrov, T. Komatsu, J. Solid State Chem. **183**, 3078 (2010)
29. G. Gao, L. Hu, H. Fan, G. Wang, K. Li, S. Feng, S. Fan, H. Chen, Opt. Mater. (Amst.) **32**, 159 (2009)
30. F.H. Margha, E.K. Radwan, M.I. Badawy, T.A. Gad-Allah, ACS Omega **5**, 14625–14634 (2020)
31. J. Hooda, R. Punia, R. S. Kundu, S. Dhankhar, N. Kishore, Int. Sch. Res. Notices **2012**, (2012).

32. S.A.M. Abdel-Hameed, M.A. Marzouk, J. Alloy. Compd. **893**, 162337 (2022)
33. F.H. ElBatal, M.A. Marzouk, J. Mater. Sci. **46**, 5140 (2011)
34. M.A. Marzouk, A.M. Abdelghany, H.A. ElBatal, Phil. Mag. **93**, 2465 (2013)
35. B. Aktas, S. Yalcin, M. Albaskara, E. Aytar, G. Ceyhan, Z.Ş Turhan, J. Non Cryst. Solids **584**, 121516 (2022)
36. B. Aktas, M. Albaskara, S. Yalcin, K. Dogru, Acta. Phys. Pol. A **132**, 442 (2017)
37. T. Akkuş, Z. Uzunoğlu, D. Yılmaz, Appl. Radiat. Isot. **145**, 7 (2019)
38. N. Sugimoto, H. Kanbara, S. Fujiwara, K. Tanaka, Y. Shimizugawa, K. Hirao, JOSA B **16**, 1904 (1999)
39. R. Kitamura, L. Pilon, M. Jonasz, Appl. Opt. **46**, 8118 (2007)
40. V. Dimitrov, S. Sakka, J. Appl. Phys. **79**, 1741 (1996)